# Maximization of the Traction Forces in a 2WD Electric Vehicle

Guillermo A. Magallan, *Student Member, IEEE*, Cristian H. De Angelo, *Senior Member, IEEE*, and Guillermo O. García, *Senior Member, IEEE*

***Abstract*—A new control strategy for obtaining the maximum traction force of electric vehicles with individual rear-wheel drive is presented. A sliding-mode observer is proposed to estimate the wheel slip and vehicle velocity under unknown road conditions by measuring only the wheel speeds. The proposed observer is based on the *LuGre* dynamic friction model and allows the maximum transmissible torque for each driven wheel to be obtained instantaneously. The maximum torque can be determined at any operating point and road condition, thus avoiding wheel skid. The proposed strategy maximizes the traction force while avoiding tire skid by controlling the torque of each traction motor. Simulation results using a complete vehicle model under different road conditions are presented to validate the proposed strategy.**

***Index Terms*—Electric vehicles (EVs), sliding-mode observers (SMOs), traction control.**

## I. Introduction

THE incorporation of traction control systems (TCSs) and antilock brake systems (ABSs) in conventional internal combustion engine vehicles (ICEVs) has significantly improved their safety and maneuverability. Such systems are based on the control of the driven wheels' longitudinal slip, thus preventing the wheels from skidding or blocking. This allows improvement of the adherence between tires and road, leading to an increase in traction forces and vehicle controllability.

Over the past few years, the combined use of both TCS and ABS in so-called electronic stability control systems has allowed vehicle stabilization in sudden maneuvers by controlling the motor torque and the braking pressure in each wheel. This way, the vehicle dynamics can be corrected to improve its stability in the face of driver maneuvers, thus decreasing the likelihood of accidents.

Traction forces, which can be effectively generated by a vehicle tire, mainly depend on the tire–road friction characteristics. During the vehicle acceleration or braking, the friction is a function of the tire slip, exhibiting a maximum for which it is possible to generate maximum traction force without skidding. If a traction torque higher than that which can be maintained by the maximum friction is applied, the wheel begins to skid, losing traction and controllability. This is the basis of traction control in vehicles.

The great development of electric vehicles (EV) and hybrid EVs (HEV) during the past few years has led to the development of new traction strategies that are more sophisticated and efficient than those used in ICEVs. Modern motor control techniques, which allow control of the electromagnetic torque of electric motors with a high dynamic response, have made this possible.

In the case of electric traction vehicles with multiple traction wheels and independent motors in each wheel, the implementation of TCS and ABS is greatly facilitated. This is due to the availability of a greater amount of manipulate variables. Such systems allow the following:

1) improving the adhesion of each of the drive wheels to the road
   a) preventing wheel skid;
   b) improving vehicle stability under changes in road conditions;
   c) improving the energy efficiency of the vehicle while avoiding losses due to skidding;
2) controlling each of the traction forces through the instantaneous torque control of each of the traction motors
   a) correcting the vehicle's dynamic behavior.

Different strategies have been developed to control the traction forces in EVs. Some of these proposals are centered in the control of the wheel slip since, as mentioned before, slip directly affects the friction coefficient. Based on this principle, some strategies that neither need the knowledge of the complete vehicle dynamics nor require a great number of sensors have been proposed.

The *Model Following Control* strategy is proposed in [1], where the dynamics of the wheel is treated as a variable-inertia system, assuming that a greater wheel slip can be seen as a lower inertia. This dynamic system is compared with the nominal plant, and the error between them is used to limit the torque applied by the traction motors to maintain the adhesion between the wheel and the road.

In the *Optimal Slip Ratio Control* [2], [3], the slip is regulated in a desired range by controlling the gradient $\partial\mu/\partial Slip$. This control strategy maintains the value of the friction coefficient slope (e.g., positive slope) bounded, which ensures the tire operating in the stable-sliding zone.

Manuscript received March 10, 2010; revised August 1, 2010; accepted October 9, 2010. Date of publication November 11, 2010; date of current version February 18, 2011. This work was supported by the National University of Río Cuarto, Agencia Nacional de Promoción Científica y Tecnológica, and Consejo Nacional de Investigaciones Científicas y Técnicas. The review of this paper was coordinated by Dr. R. Langari.

G. A. Magallan is with AMETEK Programmable Power, Inc., San Diego, CA 92121 USA (e-mail: gmagallan@ieee.org).

C. H. De Angelo and G. O. García are with the Grupo de Electrónica Aplicada (GEA), Universidad Nacional de Río Cuarto, X5804BYA, Río Cuarto, Argentina, and also with the Consejo Nacional de Investigaciones Científicas y Técnicas, C1033AAJ Buenos Aires, Argentina.

Color versions of one or more of the figures in this paper are available online at http://ieeexplore.ieee.org.

Digital Object Identifier 10.1109/TVT.2010.2091659

Based on these concepts, traction control based on controlling the ratio between the acceleration of the vehicle and the wheel is proposed in [4]. This way, the wheel slip is indirectly controlled by limiting this ratio through a relaxation factor, which is designed at a value less than 1.

Even when these strategies based on the slip limitation have demonstrated a good performance by assuring the vehicle traction at stable slip values, their operating range does not exploit the maximum transmissible traction force for a given road condition. In addition, tuning of these strategies depends on the specific road condition [4].

In other works [5]–[7], traction forces are estimated from a complete vehicle model. Such proposals allow better adaptation to different road conditions, but they require several costly sensors (accelerometers, force sensors, and yaw sensors) and a great computing capacity.

Some simpler estimation schemes based on the vehicle model have been proposed for ABS. In [8] and [9], adaptive nonlinear observers based on the one-fourth vehicle model and the *LuGre* dynamic tire model [10], which allow variations on the road condition, are proposed.

Based on these models, sliding-mode observers (SMOs) for tire friction estimation in ABS are proposed in [11] and [12]. SMOs present good characteristics for state estimation in nonlinear systems, such as robustness against parameter uncertainties and simpleness implementation. Other strategies based on SMOs and simplified vehicle models are presented in [13]. However, even when the simplifications used for the one-fourth vehicle model simplifies the implementation of the estimation strategies, this model does not represent the actual vehicle with enough fidelity. This suggests that the previously mentioned strategies can be improved.

A new strategy for traction force maximization during the acceleration of independent rear-wheel drive EV is presented in this paper. The proposed strategy is based on an SMO designed on the basis of the longitudinal vehicle dynamic and the dynamic *LuGre* friction model. This proposal requires only measuring the angular velocities of the EV wheels. From the estimated states, the maximum transmissible torque is obtained by searching the maximum value of the friction coefficient at each operating point and road condition. Dynamic saturation is used to limit the torque produced by each traction motor, thus maintaining the traction wheels in the maximum friction zone. This allows maximizing the torque and, as a consequence, obtaining the maximum traction force.

This is a remarkable difference from previously proposed strategies, which control the wheel slip. As mentioned before, even when the slip could be precisely controlled, such strategies do not exploit the maximum torque that can be transmitted in each road condition. However, the strategy proposed in this paper effectively controls the maximum transmissible torque for each road condition, thus obtaining the maximum vehicle acceleration while avoiding wheel skidding.

This paper is organized as follows: In Section II, the traction scheme is described. In Section III, the proposed control strategy is presented. In Section IV, the utilized dynamic model is described. In Section V, the design of the proposed observer is presented. In Section VI, the strategy for maximizing the traction force is introduced. In Section VII, a discussion about controller stability is made. In Section VIII, simulation results obtained under different road conditions are shown. Finally, in Section IX, conclusions are drawn.

Fig. 1. EV prototype developed at GEA-UNRC.

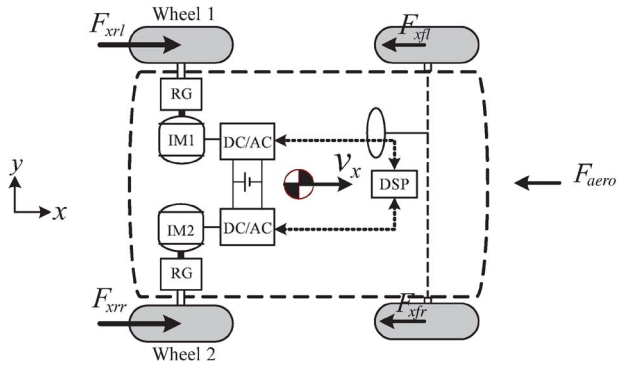


Fig. 2. EV traction scheme.

## II. Electric Vehicle Prototype and Traction Scheme

The general objective of this paper is to propose a traction control strategy that allows maximizing the traction forces of the EV prototype shown in Fig. 1. This prototype was developed at Grupo de Electrónica Aplicada, Universidad Nacional de Río Cuarto (GEA-UNRC), Argentina [14]. Fig. 2 presents a scheme of the traction system used in this EV. It has a digital signal processor, which executes the traction control algorithm. This algorithm includes two field-oriented controllers: one for each traction induction motor, which is supplied by two separate inverters (dc/ac). These motors allow applying the desired torque to each traction wheel through the reduction gears.

## III. Proposed Traction Control Strategy

The determination of the effective traction forces depends on the vehicle dynamics and the tire–road friction coefficient for each wheel. However, the friction coefficient cannot be directly determined, which is why a strategy based on an observer is proposed.

Fig. 3 shows the proposed traction control strategy. This strategy determines the maximum transmissible torque $\hat{T}_{1\max}$

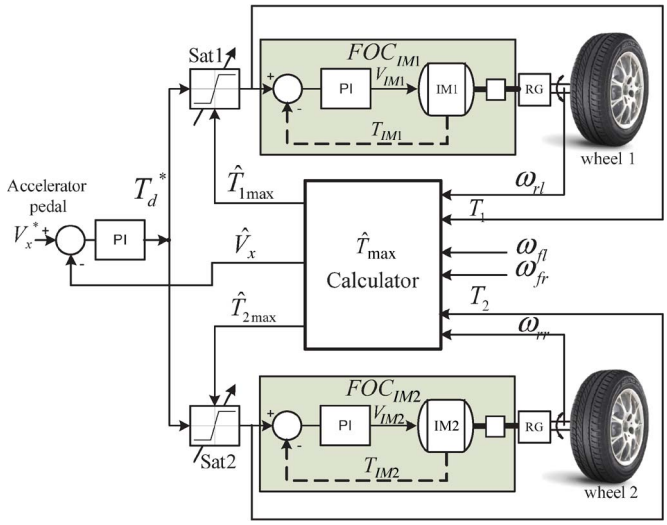


Fig. 3. Simplified scheme of the proposed traction control strategy.

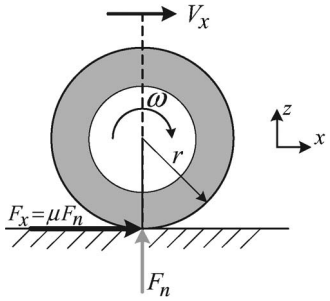


Fig. 4. Single wheel model.

and $\hat{T}_{2\max}$ from the measurement of the four wheel speeds $\omega_{fl}$, $\omega_{fr}$, $\omega_{rl}$, and $\omega_{rr}$ and the knowledge of the torque required for each traction wheel $T_1$ and $T_2$. (It is assumed that the torque required by the drive is actually applied to the wheel.)

As shown in Fig. 3, the error of the linear vehicle velocity is calculated from the reference produced by the accelerator pedal $V_x^*$ and the estimated velocity $\hat{V}_x$. This error inputs a proportional–integral (PI) regulator, whose output generates the desired torque reference $T_d^*$. The torque reference goes through amplitude saturators, whose limit values are given by $Sat_1 = \hat{T}_{1\max}$ and $Sat_2 = \hat{T}_{2\max}$. This way, if the driver requires the maximum velocity through the accelerator pedal, the torque references will be limited to the maximum value, which can be transmitted to the road, avoiding wheel skid.

## IV. Vehicle Model

In this section, the tire model and the longitudinal vehicle dynamic model used to design the observer are presented.

### A. Longitudinal Tire Model

As shown in Fig. 4, a tire–road longitudinal friction coefficient $\mu$ is defined through the ratio between the traction force $F_x$ and the normal force $F_n$

$$\mu = \frac{F_x}{F_n}. \tag{1}$$

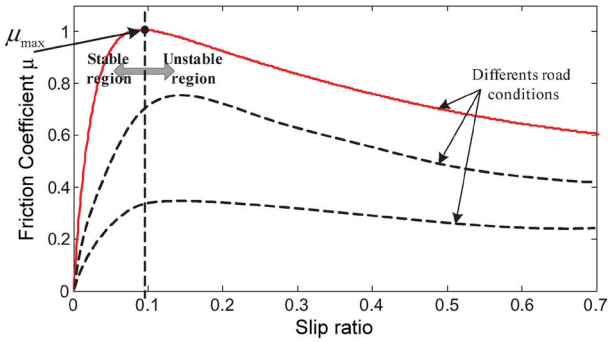


Fig. 5. Friction coefficient as a function of slip.

This friction coefficient depends on various factors, including the type of tire, the tire air pressure, the road condition, the normal forces, and the wheel slip, which is defined as

$$Slip\ ratio = \begin{cases} \frac{\omega r - V_x}{\omega r}, & \text{for driving} \\ \frac{V_x - \omega r}{V_x}, & \text{for braking} \end{cases} \tag{2}$$

where $r$ is the wheel radius, $\omega$ is the wheel angular velocity, and $V_x$ is the wheel linear velocity.

Fig. 5 shows the typical curves of the tire–road friction coefficient as a function of the slip ratio. Two well-defined operating zones can be identified in these curves. In the first one, when the torque applied to the wheel grows, the slip slowly increases while $\mu$ grows to its maximum value. At this point, the traction force transmitted by the tire to the road is the maximum. This is the normal (or stable) operating zone, where the energy transferred from the motors is transformed to traction energy with high efficiency.

Once the operating point corresponding to $\mu_{\max}$ has been reached, if the applied torque continues to increase, the wheel enters the second region of operation. In this zone, the slip grows faster while $\mu$ decreases, producing the wheel acceleration due to the reduction of the tire–road adhesion. This leads to the wheel skidding, thus losing traction control (unstable zone).

In several works, the friction coefficient is modeled through semi-empirical formulas, which reproduce the steady-state wheel behavior. One of the most used models is *The Magic Formula* (*Pacejka Model*) [15], which allows a good correlation to be obtained with experimental data for known tire and road conditions. This type of model performs a mapping between the slip and the coefficient of friction.

Usually, vehicles travel through variable road conditions; therefore, the results of empirical formulas may not represent the physical model with sufficient fidelity. On the other hand, it was proven that, with increasing vehicle speed, the friction coefficient for a given road condition decreases, which is a fact that is generally not considered in these formulas [10].

In traction control, it is necessary to consider the dynamic behavior of the friction coefficient to control the traction forces with a dynamic response that is fast enough to avoid the loss of traction (skidding).

For all these reasons, the use of a dynamic friction model is proposed in this paper. The *LuGre* dynamic friction model [10], [16] allows the adaptation to different road conditions

while representing the transient behavior of the traction force during acceleration or braking. It also considers the velocity dependence of the friction coefficient.

This model is based on considering that the tire contact with the ground is done through radial elastic bristles, which deflect when torque is applied to the wheel. This way, each element produces a longitudinal friction force component called the LuGre internal friction state $z$, which is a function of its deflection. Thus, the overall contribution of these elements on the tire contact patch produces the resultant tire friction force.

The *LuGre* dynamic model can be represented by the following equations [8]:

$$\begin{aligned} \frac{dz}{dt} &= v_r + \theta \frac{\sigma_0 |v_r|}{g(v_r)} \cdot z - \kappa \cdot r|\omega| \cdot z \\ g(v_r) &= \mu_C + (\mu_S - \mu_C) \cdot e^{-\left|\frac{v_r}{v_s}\right|} \\ F_x &= \left( \sigma_0 \cdot z + \sigma_1 \cdot \frac{dz}{dt} + \sigma_2 \cdot v_r \right) \cdot F_n \end{aligned} \tag{3}$$

where

| | |
|---|---|
| $\sigma_0$ | normalized rubber longitudinal lumped stiffness $[1/m]$; |
| $\sigma_1$ | normalized rubber longitudinal lumped damping $[s/m]$; |
| $\sigma_2$ | normalized viscous relative damping $[s/m]$; |
| $\mu_C$ | normalized Coulomb friction $[-]$; |
| $\mu_S$ | normalized static friction $[-]$; |
| $v_s$ | Stribeck relative velocity $[m/s]$; |
| $\kappa$ | force distribution parameter $[1/m]$; |
| $v_r = \omega r - V_x$ | relative velocity $[m/s]$; |
| $z$ | internal friction state $[m]$; |
| $\theta$ | road condition parameter $[-]$. |

An important characteristic of this model is that different values of the $\theta$ parameter allow reproduction of different road conditions (see Fig. 5).

### B. Longitudinal Vehicle Model

By considering only the longitudinal vehicle movement, as shown in Fig. 2, and using the *LuGre* model for determining the traction forces, the vehicle dynamics can be represented as follows:

$$\dot{V}_x = \frac{1}{m} \cdot (F_{xrl} + F_{xrr} + F_{xfl} + F_{xfr} + F_{\text{aero}}) \tag{4}$$

$$\begin{aligned} \dot{\omega}_{rl} &= \frac{1}{J_r} \cdot (-F_{xrl} \cdot r - \sigma_\omega \cdot \omega_{rl} + T_1) \\ \dot{\omega}_{rr} &= \frac{1}{J_r} \cdot (-F_{xrr} \cdot r - \sigma_\omega \cdot \omega_{rr} + T_2) \\ \dot{\omega}_{fl} &= \frac{1}{J_f} \cdot (-F_{xfl} \cdot r - \sigma_\omega \cdot \omega_{fl}) \\ \dot{\omega}_{fr} &= \frac{1}{J_f} \cdot (-F_{xfr} \cdot r - \sigma_\omega \cdot \omega_{fr}) \end{aligned} \tag{5}$$

where subscripts $rl$, $rr$, $fl$, and $fr$ mean rear-left, rear-right, front-left, and front-right, respectively; $m$ is the vehicle mass; $J_r$ and $J_f$ are the rear and front wheels' inertia, respectively; $\sigma_\omega$ is the viscous friction coefficient of the wheel axis; $T_1$ and $T_2$ are the torques applied to the driven wheels; and $F_{\text{aero}}$ is the aerodynamic force.

From (3), the individual traction forces can be determined as follows:

$$\begin{aligned} F_{x(ij)} &= F_{n(ij)} \cdot (\sigma_0 \cdot z_{ij} + \sigma_1 \cdot \dot{z_{ij}} + \sigma_2 \cdot v_{rij}) \\ \{ij\} &= rl, rr, fl, fr. \end{aligned} \tag{6}$$

The aerodynamic force is modeled through the following empirical formula:

$$F_{\text{aero}} = -C_x \cdot \rho_{\text{air}} \cdot A_f \cdot {V_x}^2 \tag{7}$$

where $C_x$ is the aerodynamic coefficient, $\rho_{air}$ is the air density, and $A_f$ is the effective vehicle frontal area.

## V. Proposed Observer

Previous strategies that use observers based on the *LuGre* model have been proposed for estimating the tire–road friction coefficient, mainly in ABS [8], [9], [11], [12]. These works are based on a simplified one fourth vehicle model, where the dynamic of each wheel is considered as independent of the rest of the vehicle, neglecting their interaction with the other wheels and affected only by one fourth of the total mass of the vehicle.

The mentioned simplified models do not always accurately represent the physical system. For this reason, from the available measurements, an observer based on a more complete model that considers the interaction between the four wheels is proposed in this paper.

As mentioned before, the proposed traction control strategy is based on an observer designed using a complete vehicle model that allows calculation of the maximum torque that each traction wheel can transmit to the road at each instant. To the best of the authors' knowledge, there is no proposal in the literature like that presented in this paper for traction control.

The vehicle dynamic model (3)–(7) is highly nonlinear, with a large number of parameters that are difficult to determine. Such parameters can vary in a wide range influenced by different factors, which can be considered to be external perturbations.

SMOs have demonstrated to be very efficient when used in nonlinear systems because they are robust under parameter variations and easy to implement with a low computational burden. In addition, it is possible to design an SMO considering the model nonlinearities as unknown inputs, being necessary to know only the bound of the nonlinear terms [17]. For all these reasons, an SMO was chosen to implement the proposed traction control strategy.

Since the EV prototype has rear-wheel traction, the estimation of only the variables necessary to control the traction forces of these wheels is proposed. The forces on the front wheels (nondriven wheels) are calculated from the measurement of their angular velocities as follows:

$$F_{xfi} = \frac{-1}{r} \cdot (\sigma_\omega \omega_{fi} + J_f \dot{\omega}_{fi}), \qquad i = l, r. \tag{8}$$

From the complete vehicle model (3)–(7), the following state variables are defined:

$$\begin{bmatrix} x_1 \\ x_2 \\ x_3 \\ x_4 \\ x_5 \end{bmatrix} = \begin{bmatrix} z_{rl} \\ z_{rr} \\ V_x \\ r\omega_{rl} - V_x \\ r\omega_{rr} - V_x \end{bmatrix}$$

where $z_{rl}$ and $z_{rr}$ correspond to the internal friction states of the *LuGre* model for each driven wheel.

By approximating the traction forces in (5) by $F_{x(ij)} \cong F_n \cdot (\sigma_0 \cdot z_{ij} + \sigma_1 \cdot \dot{z}_{ij})$ [8], the vehicle dynamics can be represented as follows, where the linear and nonlinear terms have been separated:

$$\begin{aligned} \dot{\mathbf{x}} &= \mathbf{A}\mathbf{x} + \mathbf{B}\mathbf{u} + \mathbf{D}\mathbf{f}(\mathbf{x}) \\ \mathbf{y} &= \mathbf{C}\mathbf{x} \end{aligned} \tag{9}$$

where

$$\mathbf{A} = \begin{bmatrix} 0 & 0 & 0 & 1 & 0 \\ 0 & 0 & 0 & 0 & 1 \\ \frac{F_{n1}\sigma_0}{m} & \frac{F_{n2}\sigma_0}{m} & 0 & a_{34} & a_{35} \\ q_1\sigma_0 & \frac{-F_{n1}\sigma_0}{m} & \frac{-\sigma_\omega}{J_r} & a_{44} & a_{45} \\ \frac{-F_{n1}\sigma_0}{m} & q_2\sigma_0 & \frac{-\sigma_\omega}{J_r} & a_{54} & a_{55} \end{bmatrix}$$

$$a_{34} = \frac{F_{n1}}{m}(\sigma_1 + \sigma_2) \quad a_{35} = \frac{F_{n2}}{m}(\sigma_1 + \sigma_2)$$

$$a_{45} = -a_{35} \quad a_{54} = -a_{34}$$

$$a_{44} = q_1\sigma_1 - \frac{F_{n1}\sigma_2}{m} - \frac{\sigma_\omega}{J_r}$$

$$a_{55} = q_2\sigma_1 - \frac{F_{n2}\sigma_2}{m} - \frac{\sigma_\omega}{J_r}$$

$$q_1 = -F_{n1}\left(\frac{r^2}{J_r} + \frac{1}{m}\right) \quad q_2 = -F_{n2}\left(\frac{r^2}{J_r} + \frac{1}{m}\right)$$

$$\mathbf{B} = \begin{bmatrix} 0 & 0 & 0 & 0 & 0 \\ 0 & 0 & 0 & 0 & 0 \\ 0 & 0 & \frac{1}{m} & \frac{1}{m} & \frac{1}{m} \\ \frac{r}{J_r} & 0 & \frac{-1}{m} & \frac{-1}{m} & \frac{-1}{m} \\ 0 & \frac{r}{J_r} & \frac{-1}{m} & \frac{-1}{m} & \frac{-1}{m} \end{bmatrix} \quad \mathbf{u} = \begin{bmatrix} T_1 \\ T_2 \\ F_{\text{aero}} \\ F_{xfl} \\ F_{xfr} \end{bmatrix}$$

$$\mathbf{D} = \begin{bmatrix} -1 & 0 \\ 0 & -1 \\ \frac{-F_{n1}\sigma_1}{m} & \frac{-F_{n2}\sigma_1}{m} \\ -q_1\sigma_1 & \frac{F_{n2}\sigma_1}{m} \\ \frac{F_{n1}\sigma_1}{m} & -q_2\sigma_1 \end{bmatrix}$$

$$\mathbf{f}(\mathbf{x}) = \begin{bmatrix} (\theta_1 f(x_4) + \kappa(x_4 + x_3))\, x_1 \\ (\theta_2 f(x_5) + \kappa(x_5 + x_3))\, x_2 \end{bmatrix}$$

$$f(x_4) = \frac{\sigma_0|x_4|}{g(x_4)} \quad f(x_5) = \frac{\sigma_0|x_5|}{g(x_5)}$$

$$\mathbf{C} = \begin{bmatrix} 0 & 0 & \frac{1}{r} & \frac{1}{r} & 0 \\ 0 & 0 & \frac{1}{r} & 0 & \frac{1}{r} \end{bmatrix}$$

with $F_{n1}$ and $F_{n2}$ being the normal forces correspondent to the left and right rear wheels, respectively, and $\theta_1$ and $\theta_2$ being the parameters of the *LuGre* model, which represent the road condition at each wheel.

The outputs (measurements) of the system (9) are the rear wheel speeds $\omega_{rl}$ and $\omega_{rr}$. This system is used in the next section to design the observer to be used in the traction control strategy.

### A. Observer Design

From the vehicle dynamic model (9) and assuming that the wheels' angular velocities are measured, the following SMO is proposed:

$$\dot{\hat{\mathbf{x}}} = \mathbf{A}\hat{\mathbf{x}} + \mathbf{B}\mathbf{u} + \mathbf{L}\mathbf{e}_y + \mathbf{D}\nu \tag{10}$$

with $\mathbf{L}$ being a constant gain matrix, $\mathbf{e}_y$ being the output estimation error given by

$$\mathbf{e}_y = \begin{bmatrix} e_{y1} \\ e_{y2} \end{bmatrix} = \begin{bmatrix} \omega_{rl} - \hat{\omega}_{rl} \\ \omega_{rr} - \hat{\omega}_{rr} \end{bmatrix}$$

and $\nu$ being a discontinuous vector function used to induce the sliding motion

$$\nu = \begin{cases} k\frac{\mathbf{F}\mathbf{e}_y}{\|\mathbf{F}\mathbf{e}_y\|_2}, & \text{for } \mathbf{F}\mathbf{e}_y \neq \mathbf{0} \\ \mathbf{0}, & \text{for } \mathbf{F}\mathbf{e}_y = \mathbf{0} \end{cases}$$

where $k$ and $\mathbf{F}$ are the design parameters. In this observer structure, once the sliding motion is established, the term $\mathbf{D}\nu$ represents the system nonlinearities $\mathbf{f}(\mathbf{x})$, nonmodeled dynamics (e.g., vertical dynamics effects), and parameter uncertainties.

Since the pair $(\mathbf{A}, \mathbf{C})$ in (9) is observable and the nonlinear term is bounded ($\|\mathbf{f}(\mathbf{x})\| \leq \rho \in \mathbb{R}^2$), it is possible to find matrices $\mathbf{L}$ and $\mathbf{F}$ in (10) such that the state estimation error ($\mathbf{e} = \mathbf{x} - \hat{\mathbf{x}}$) is asymptotically stable [17].

Different constructive methods have been proposed to find these matrices [18], [19]. In this paper, $\mathbf{L}$ and $\mathbf{F}$ were determined, following the procedure proposed in [17, Sec. VIII].

Since $\text{rank}(\mathbf{C}\mathbf{D}) = \text{rank}(\mathbf{D}) = 2$, it is possible to find nonsingular matrices that allow the transformation of the system (9) to the particular form proposed in [17]. From the transformed system, it is possible to calculate matrix gain $\mathbf{L}$, which allows placing the eigenvalues of $(\mathbf{A} - \mathbf{L}\mathbf{C})$ in the open left-half plane, and matrices $\mathbf{P}$ and $\mathbf{F}$, which satisfy

$$(\mathbf{A} - \mathbf{L}\mathbf{C})^T\mathbf{P} + \mathbf{P}(\mathbf{A} - \mathbf{L}\mathbf{C}) = -\mathbf{Q} \tag{11}$$

$$\mathbf{F}\mathbf{C} = \mathbf{D}^T\mathbf{P} \tag{12}$$

with $\mathbf{Q} = \mathbf{Q}^T$ being positive definite to meet the Lyapunov stability criteria. Finally, $k$ is chosen such that $k \geq \rho$, which ensures a stable sliding motion, and that the estimation error goes to zero in a finite time.

## VI. Maximization of the Traction Forces

The maximum forces produced by each drive wheel depend on the maximum value of the individual friction coefficient. From the states estimated by the observer, it is possible to determine the road condition at any instant. Then, the steady-state curve of the friction coefficient can be calculated, which

allows the maximum friction at each operating point to be obtained. With this value, the torque that must be applied by the motor to produce the maximum traction force that can be obtained. This procedure is described in the following sections.

### A. Determination of the Road Condition

Different road conditions are represented by parameter $\theta$ in model (3). This parameter can be calculated from the observer estimates as described here.

Once in the sliding motion, since the estimation error tends to zero $(e \to 0)$, the equivalent output error injection signal $\mathbf{D}\nu_{eq}$ necessary to maintain the sliding motion is equal to the nonlinear term $\mathbf{Df}(\mathbf{x})$ of (10) [11], [20]. Thus

$$\nu_{1eq} = \left(\theta_1 \frac{\sigma_0|x_4|}{g(x_4)} + \kappa(x_3 + x_4)\right) x_1$$

$$\nu_{2eq} = \left(\theta_2 \frac{\sigma_0|x_5|}{g(x_5)} + \kappa(x_3 + x_5)\right) x_2. \tag{13}$$

Since the estimated variables converge to the actual variables, the estimation of $\hat{\theta}_1$ and $\hat{\theta}_2$ can be obtained from (13) as follows:

$$\hat{\theta}_1 = \left(\frac{\nu_{1eq}}{\hat{x}_1} - \kappa(\hat{x}_3 + \hat{x}_4)\right) \frac{g(\hat{x}_4)}{\sigma_0|\hat{x}_4|}$$

$$\hat{\theta}_2 = \left(\frac{\nu_{2eq}}{\hat{x}_2} - \kappa(\hat{x}_3 + \hat{x}_5)\right) \frac{g(\hat{x}_5)}{\sigma_0|\hat{x}_5|}. \tag{14}$$

To obtain valid information from (14), a nonnull slip at the traction wheels is necessary ($\hat{x}_4 \neq 0$ and $\hat{x}_5 \neq 0$). When the vehicle is not accelerating $(Slip \approx 0)$, parameter $\hat{\theta}$ is set at its nominal value $\hat{\theta} = \hat{\theta}_{nom}$, since in such circumstances, there is no risk of wheel skidding.

### B. Estimation of the Maximum Transmissible Torque

To obtain the steady-state tire–road friction curve $\mu_{ss}(slip)$ from parameter $\theta$, the steady-state *LuGre* model is used. This model can be obtained from (3) by considering $\dot{z} \cong 0$ [10]

$$z_{ss} = \frac{v_r}{\frac{\theta\sigma_0|v_r|}{g(v_r)} + \kappa r|\omega|}$$

$$\mu_{ss} = \frac{\sigma_0 v_r}{\frac{\theta\sigma_0|v_r|}{g(v_r)} + \kappa r|\omega|} + \sigma_2 v_r \tag{15}$$

where $z_{ss}$ and $\mu_{ss}$ represent $z$ and $\mu$ in steady state, respectively.

The curve $\mu_{ss}$ as a function of the slip can be obtained from (15) as a family of curves parameterized in $V_x$. By replacing $\omega = (v_r + V_x)/r$ in (15), the steady-state friction coefficient can be obtained for a given $V_x$, i.e.,

$$\mu_{ss}(v_r) = \frac{\sigma_0 v_r}{\frac{\theta\sigma_0|v_r|}{g(v_r)} + \kappa(v_r + V_x)} + \sigma_2 v_r. \tag{16}$$

To get the maximum traction force, it is necessary to calculate the maximum of $\mu_{ss}$ in (16), i.e., $\mu_{ss\max}$. It can be demonstrated that, for the range of parameters used in practice, $\mu_{ss\max}$ is not significantly affected by $\sigma_2 v_r$. Thus, this term can be neglected in (16). The maximum can be obtained from $(\partial\mu_{ss}/\partial v_r) = 0$, which results in

$$\kappa V_x g(v_r)^2 - \frac{\sigma_0\theta v_r^2}{v_s}\left(g(v_r) - \mu_C\right) = 0. \tag{17}$$

To calculate the value of the relative velocity $v_{r\max}$, which corresponds to $\mu_{ss\max}$, the exponential term of $g(v_r)$ is approximated by a second-order Taylor polynomial. This approximation allows the maximum of (16) to be obtained from the roots of a fourth-order polynomial.

Once $v_{r\max}$ was found, $\mu_{ss\max}$ can be obtained by evaluating (16) in this value.

Finally, the maximum torque that can be applied by each traction motor can be estimated from (5) in steady state, i.e.,

$$\hat{T}_{\max} = \hat{\mu}_{ss\max} F_n r + \sigma_\omega \frac{(v_{r\max} + \hat{x}_3)}{r}. \tag{18}$$

It must be noted that both the observer and the maximum torque calculation strategy need the knowledge of the normal force $F_n$. Such force may significantly vary, depending on the vertical vehicle dynamics (suspension rigidness). However, the measurement of this variable requires the use of force sensors in each wheel.

However, this complication is avoided with the use of the proposed observer. The rated normal force is used as a parameter in the observer equations and in the maximum torque calculation. Actual normal force variations are compensated by the observer, which is the same as the nonlinear terms in (9). This will produce a difference in the estimation of the road condition and, as a consequence, in the calculus of $\mu_{ss\max}$. However, the observer convergence assures the correct estimation of the product $\mu F_n$ in both the observer and the maximum torque calculation. Thus, such a torque value used to limit the motor torque will be correctly calculated, even under variations in the normal forces. The only requirement is that the estimation error dynamics must be an order faster than the vertical dynamics.

The proposed strategy for calculating the maximum torque, which corresponds to the block "$T_{\max}$ calculator" in Fig. 3, is summarized in Fig. 6.

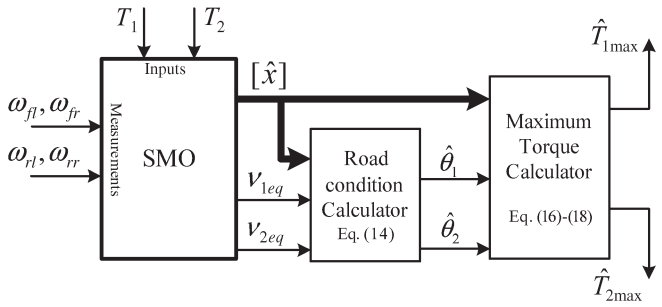


Fig. 6. Scheme of the strategy proposed for determining the maximum transmissible torque.

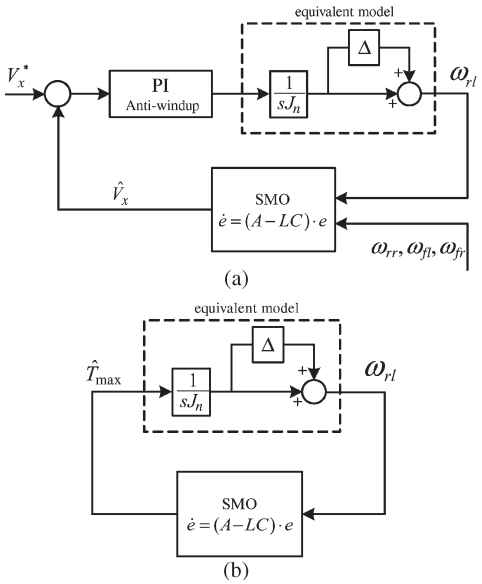


Fig. 7. (a) Control system without torque saturation (good adherence condition). (b) Control system under torque saturation (bad adherence condition).

## VII. Discussion

Even when the wheel dynamics and its interaction with the road is complex and nonlinear, for the purpose of stability analysis, the system can be modeled as shown in [4]. In this equivalent model, a parameter $\Delta$ is introduced to take into account the undertransmitted torque under wheel slip conditions. This allows considering the skid phenomenon as a variation of the system inertia ($\Delta = J_n/(J-1)$). Under good tire adherence condition, $\Delta = 0$, and the vehicle dynamics is affected by its nominal inertia $J_n = J_w + Mr^2$. However, under conditions of extreme tire skidding, $\Delta = (Mr^2/J_w)$, and the vehicle dynamics is affected only by the wheel inertia (see [4] and references therein).

Regarding the proposed controller stability, the analysis can be divided into two parts: The first one corresponds to the system under good adherence conditions, where the torque saturation is not acting, whereas the second one corresponds to the system dynamics when torque saturation acts.

While torque saturation does not constrain the controller output, the equivalent closed-loop system is as shown in Fig. 7(a). The blocks that interact are the following: the PI regulator that controls the linear speed of the vehicle, the equivalent model, and the loop that is closed through the SMO observer. The SMO design matrices (based on the procedure [17]) lead the observer to the sliding surface. Once the SMO reached this condition, the estimation error dynamics $(\mathbf{x} - \hat{\mathbf{x}})$ is governed only by the linear part of system, i.e., the eigenvalues of $(\mathbf{A} - \mathbf{LC})$. Since, in this paper, gain $\mathbf{L}$ was chosen so as these eigenvalues lie in the left-half plane, we can ensure that the error converges to zero in a finite time. Thus, we know that $\hat{V}_x \to V_x$ in a finite time and that the PI regulator can be tuned to obtain the desired dynamic response based on the simple equivalent model.

It is worth noting here that the estimate $\hat{V}_x$ is not obtained from direct measurement of the velocities of the front wheels, but it is estimated using the measurement of the four wheel velocities and rear wheels torques, including the overall longitudinal dynamics. The latter allows a more accurate estimate of $V_x$ and allows the improvement of the control robustness (e.g., even when one of the front wheels is skidding, a good estimation of $V_x$ can be obtained).

When torque saturation acts, the equivalent control system results as shown in Fig. 7(b). In this case, the velocity PI controller is removed, and the control loop is closed directly with the estimated torque saturation value, which is obtained from the maximum torque calculator ($\hat{T}_{\max}$). In the same way as in the case without saturation, once the SMO is in the sliding surface, the estimation error dynamics depends on the eigenvalues of $(\mathbf{A} - \mathbf{LC})$, and therefore, the error asymptotically tends to zero. Then, a stable operation of the system in this case can be obtained by properly setting the observer gain $\mathbf{L}$

## VIII. Simulation Results

To demonstrate the practical feasibility of the theoretical proposal made in this paper, the complete system was modeled, and its behavior under different conditions was simulated. Modeling of all the mechanical components (chassis, suspension, and wheels) and the traction motors was performed using *Bond Graph* formalism in *Dymola* environment [21]. On the other hand, the traction control algorithm was designed and programmed using block diagrams under *Simulink* environment. Since two different methodologies were used to implement the physical model and its control, a hybrid simulation scheme combining *Simulink* and *Dymola* was used. The complete vehicle model programmed into the *Dymola* environment [22] is run by *Simulink* through an *S-function* block. This allows access to all the measurement and control signals of the vehicle by running the complete simulation in *Simulink*.

The mechanical parameters used in the simulations correspond to the EV prototype shown in Table I.

To reproduce different road conditions during the simulations, different values of $\theta$ were set in the *LuGre* models of each vehicle wheel. In particular, a sudden change in the road condition was simulated by changing from $\theta = 1$ to $\theta = 3$, which corresponds to a good adherence road (dry asphalt) and a slippery road (snowy asphalt), respectively. These conditions will be referred to, from now on, as tire–road conditions $\mu_1$ and $\mu_2$, respectively.

The actual parameters of the *LuGre* model, which are necessary in implementing the observer, can be experimentally obtained through acceleration tests of the vehicle by measuring the values of $T_{ri}$, $F_{ni}$, $V_x$, and $\omega_i$ for a known road condition. The *LuGre* model parameters used in this paper are presented in Table I.

With these parameters and following the procedure described in Section V-A with a rated normal force $F_n = 1900$ N, the following observer gains were adjusted:

$$\mathbf{L} = \begin{bmatrix} -3.47 & 0 \\ 0 & -3.47 \\ -44.8 & -44.8 \\ 1008.35 & 44.8 \\ 44.8 & 1008.35 \end{bmatrix}, \quad \mathbf{F} = \begin{bmatrix} 1039.1 & 0 \\ 0 & 1039.1 \end{bmatrix}.$$

Some results of the simulation experiment are presented here.

TABLE I
VEHICLE PARAMETERS

| | |
|---|---|
| Vehicle mass ($m$) | 590 Kg |
| Tires, type and size | 145 70 R13 S |
| Distance between wheels | 1.10 m |
| Distance CG to frontal axis | 1.02 m |
| Distance CG to rear axis | 0.68 m |
| Tire radio (with no load) ($r$) | 0.2666 m |
| Unsprung mass (w/ wheel) ($m_w$) | 38.42 Kg |
| Tire vertical rigidness | 150000 N/m |
| Wheel inertia ($J_r$, $J_f$) | 1.95 Kgm$^2$ |
| Suspension damper coefficient | 2400 Ns/m |
| Suspension rigidness | 10600 N/m |
| Yaw inertia | 352 Kgm$^2$ |
| Pitch inertia | 356 Kgm$^2$ |
| Roll inertia | 152 Kgm$^2$ |
| Aerodynamic coefficient ($C_x$) | 0.5 |
| Frontal area ($A_f$) | 1.4 m$^2$ |
| Air density ($\rho_{air}$) | 1.225 Kg/m$^3$ |
| $\sigma_0$ | 150 1/m |
| $\sigma_1$ | 4 s/m |
| $\sigma_2$ | 0.01 s/m |
| $\mu_C$ | 0.3 |
| $\mu_S$ | 1.4 |
| $v_s$ | 1.5 m/s |
| $L$ | 0.2 m |
| $\kappa$ | $\frac{7}{6L}$ 1/m |

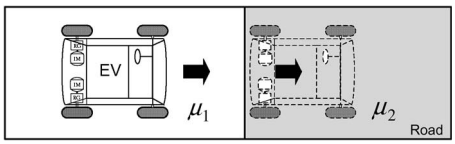


Fig. 8. Road of experiment A.

### A. Vehicle Acceleration Under Different Road Conditions

As shown in Fig. 8, in this experiment, the vehicle travels a straight path, initially in a tire–road condition $\mu_1$, and then suddenly switches to a $\mu_2$ condition. Fig. 9 shows the evolution of the variables for this experiment.

Fig. 9(a) shows the reference linear velocity, the actual vehicle velocity, and the estimated velocity. As it can be seen, from $t = 0$ s to $t = 1$ s, the vehicle is traveling at a constant speed (1 m/s) on the road condition $\mu_1$. From there, it begins to accelerate with a reference speed $V_x^* = 6$ m/s, which is maintained until $t = 2.5$ s. At this point, the reference speed is changed to $V_x^* = 10$ m/s, and the vehicle begins accelerating again, still on the road condition $\mu_1$. At $t = 3$ s, the rear wheels enter the $\mu_2$ road condition. As can be appreciated, there is practically no error between the estimated and the actual velocity. This allows the use of the estimated velocity to implement the vehicle control strategy without requiring expensive sensors.

The motor torque and the action of the dynamic saturation are shown in Fig. 9(b). Such saturation limits the applied torque to the maximum motor torque in the case of good adherence conditions or to the maximum transmissible torque if necessary to avoid wheel skidding.

Initially, the applied torque is very small, because the vehicle is traveling at constant speed. At $t = 1$ s, when the reference velocity is changed, the applied torque grows until it is limited by the dynamic saturation. This causes the operating point to move to the corresponding maximum friction coefficient, as shown in Fig. 9(c). It can also be observed in Fig. 9(d)

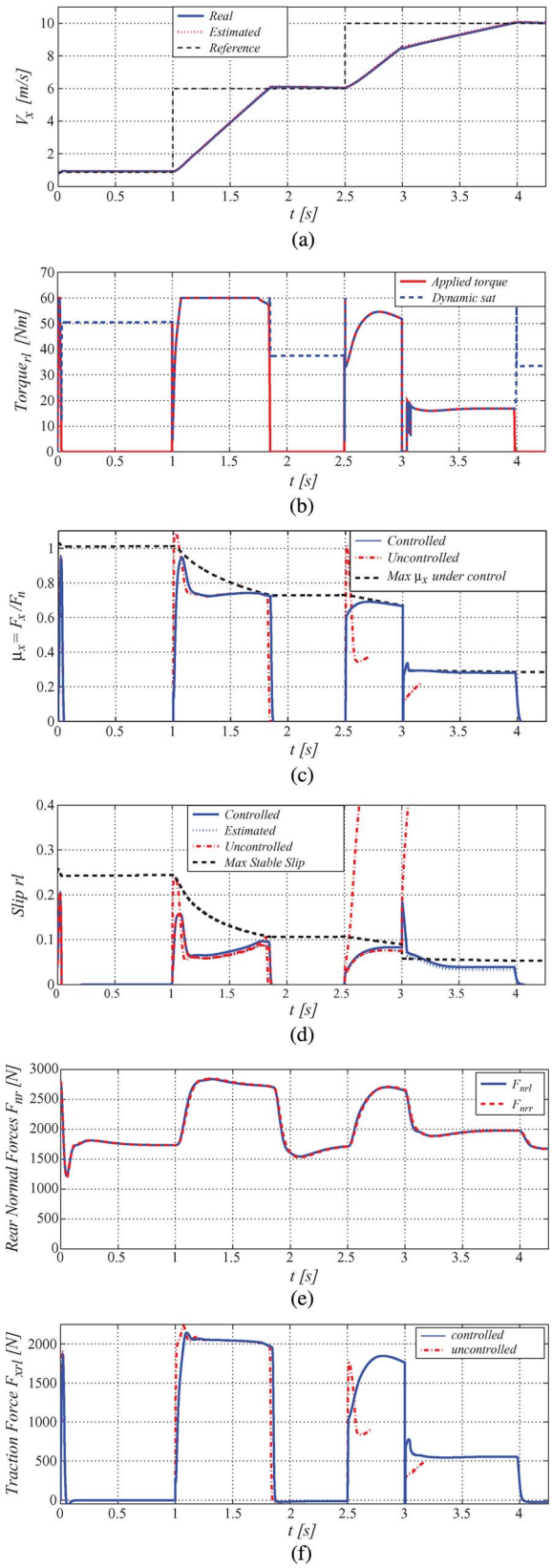


Fig. 9. Experiment A. (a) Linear velocity. (b) Torque applied by the motors. (c) Friction coefficient. (d) Slip. (e) Rear normal forces. (f) Traction forces.

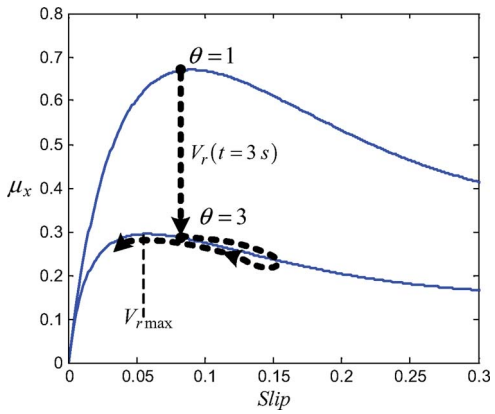


Fig. 10. Steady-state friction curves at the change in the road conditions ($t = 3$ s, $v_x = 8.5$ m/s).

that the slip is maintained in the stable zone during this first acceleration.

After the transient previously described, the dynamic torque saturation allows applying the rated motor torque (60 Nm). At about $t = 1.7$ s, the dynamic saturation acts again since the maximum friction coefficient is reached [see Fig. 9(c)].

At $t = 1.85$ s, the vehicle reaches the reference velocity given by the accelerator pedal ($V_x^* = 6$ m/s), making the applied torque decrease to a minimum.

It can be appreciated that, between $t = 2.5$ s and $t = 3$ s (second acceleration), the dynamic torque saturation allows the friction coefficient to evolve toward its maximum value while the slip is maintained in the stable zone [see Fig. 9(d)].

At $t = 3$ s, the sudden change in the road condition from $\mu_1$ to $\mu_2$ occurs. This change in the road condition produces a transition in the operating point, as shown in Fig. 10. At the time of transition, the road condition instantaneously changes while the slip remains constant since it depends on the dynamics of the wheel. As a consequence, the new operating point is on the unstable zone.

Given this transition, the observer adapts to the new road condition, and the maximum friction point for this condition is calculated. When it is detected that $\hat{v}_r > \hat{v}_{r\max}$, the traction control algorithm sets the torque reference at $T^* = 0$ to bring the operating point to the stable zone. Once $v_r <= \hat{v}_{r\max}$, the control algorithm returns to its normal operation by applying the maximum traction torque in this new condition.

As shown in Fig. 9(c) and (d), from $t = 3$ s, the friction coefficient sharply drops while the slip rapidly increases, exceeding its maximum stable value. Fig. 9(b) shows that, when the change in the road condition has occurred and the transition to an unstable operation zone has been detected, the control reduces the applied torque to zero, bringing the operating point to the stable operation area. Once it has come back to the stable operation zone, dynamic saturation acts, maintaining the value of the maximum torque for this new road condition from $t = 3.05$ s to $t = 4$ s, as shown in Fig. 9(b).

Fig. 9(c) shows the evolution of the normal forces on the traction wheels during this experiment. An increase in these forces can be appreciated when the vehicle accelerates, due to the pitch movement produced by the load displacement. This effect directly affects the traction forces [see Fig. 9(f)].

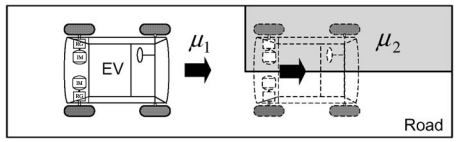


Fig. 11. Road of experiment B.

To appreciate the benefits of the proposed traction control, the transient signals without traction control for certain operating points of the experiment are shown in the figures previously described in superimposed form (dash-dotted line). Fig. 9(c) shows that, at $t = 1$ s, a higher friction $\mu$ is produced, because the application of maximum motor torque generates higher load shifting backward (pitch movement) by increasing the rear normal forces, which allows supporting a traction force that is greater than that obtained under control. On the other hand, as shown in Fig. 9(d), the slip reaches the unstable zone in this case, which may cause the drive wheels to skid.

For the second acceleration in the uncontrolled case (from $t = 2.5$ s), it can be clearly seen in Fig. 9(d) that the wheel begins to skid, accelerating and increasing the slip and, thus, losing adherence. This causes the reduction of the traction force, as shown in Fig. 9(f).

At the change in the road condition ($t = 3$ s), if the traction control is not active, the wheel starts skidding from $t = 3$ s, and the traction force decreases, as shown in Fig. 9(d) and (f).

The results of this experiment show that the proposed control strategy is able to assure the vehicle traction at any time, taking advantage of the maximum coefficient of friction under every road condition, if necessary, and keeping both wheels' slip in the stable range. A good estimation of the traction forces, even on low adherence road conditions, can also be verified in Fig. 9(f).

### *B. Changing the Road Condition on One Side of the Vehicle*

During this experiment, as shown in Fig. 11, the left half of the vehicle passes through a change in the road conditions (from $\mu_1$ to $\mu_2$), whereas the right half remains in the road condition $\mu_1$.

The vehicle starts in the same conditions of experiment A, and the same reference signals from the accelerator pedal are applied. A significant difference can be observed from $t = 3$ s in Fig. 12(b) and (c). A differential torque is applied from there, due to the difference in the road conditions of each wheel. Fig. 12(d) and (e) show that the proposed control allows tracking of the maximum friction coefficient in each wheel, maximizing the individual traction force. After the change in road condition, the drive wheels are at different values of the friction coefficient, which produces different traction forces, generating, as a consequence, a yaw moment, as shown in Fig. 12(f). Fig. 13(a) and (b) show that the slip in each drive wheel is kept in the stable operating region during this experiment.

### *C. Safe Traction by Applying Equal Traction Force (Yaw Rate Reduction)*

As shown in experiment B, the significant difference between the traction forces when the wheels operate with different

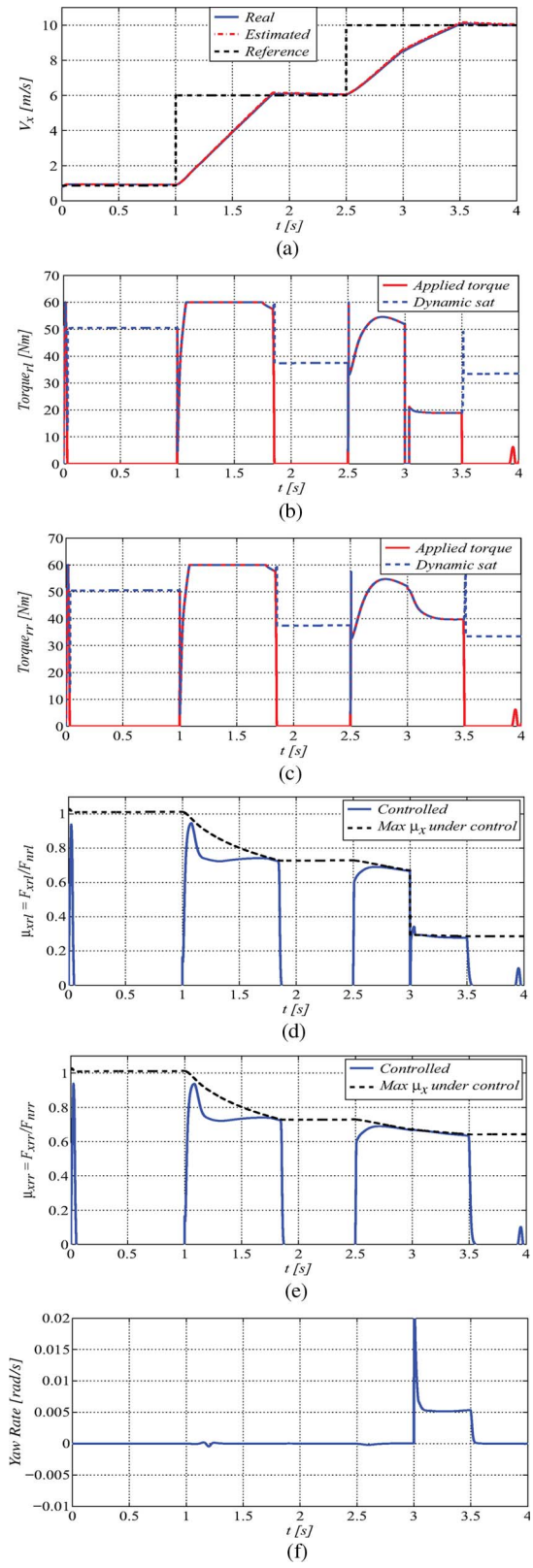


Fig. 12. Experiment B. (a) Linear velocity. (b) Rear-left wheel torque. (c) Rear-right wheel torque. (d) Rear-left wheel friction. (e) Rear-right wheel friction. (f) Yaw rate.

road conditions generates a yaw moment, which, under certain circumstances, may be dangerous for the driver. Under these circumstances, a possible strategy to increase vehicle stability

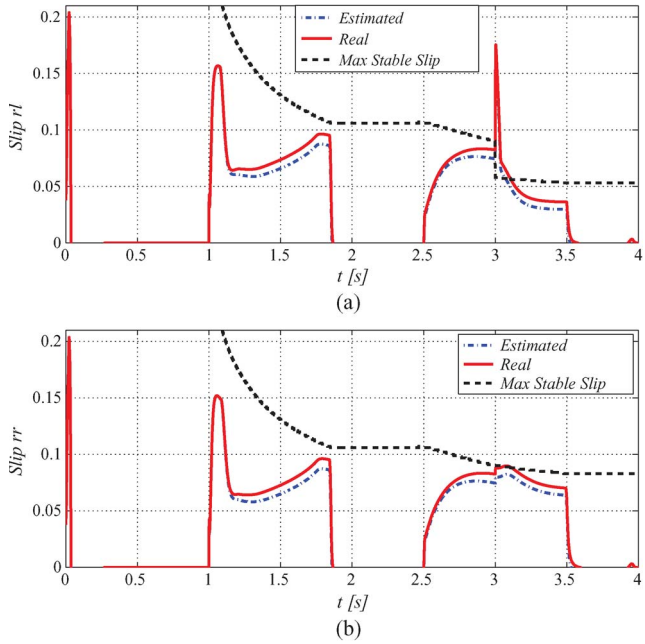


Fig. 13. Experiment B. Slip of (a) the wheel with change in road condition and (b) the wheel without change in road condition.

is to set the torque saturation of both wheels equal to the lesser of the maximum torques that determines the traction control to each wheel. This action, on the one hand, prevents the wheel with less adherence from skidding and, on the other hand, takes the wheel with greater adherence to an operating point of less slippage, producing an equal force of traction on both wheels and consequently decreasing the yaw moment.

To verify the operation of this strategy, an equal traction force was implemented for the same conditions of experiment B. As can be appreciated from Fig. 14(b) and (c), this strategy produces the same friction coefficient in both wheels all the time, which implies equal traction forces in each wheel. Fig. 14(d) shows that the yaw rate is significantly reduced when compared with Fig. 12(f). This occurs at the expense of losing acceleration of the vehicle. The evolution of slip on the two wheels is shown in Fig. 14(e) and (f), showing a significant reduction in the rear right wheel slip, because this wheel has a larger adhesion.

## IX. Conclusion

A new strategy for traction control of EVs with independent rear wheel drive has been presented in this paper. This strategy is based on an SMO built from the longitudinal vehicle model, including the dynamic friction LuGre model to estimate forces in each of the drive wheels and the vehicle velocity. From the estimated variables, the maximum of the tire–road friction curve at each operating point has been determined. Then, the maximum torque that can be applied to each wheel for each operating point and road condition has been calculated. This value has been used to limit the motor torque, thus avoiding the wheel skidding and the vehicle loss of traction and stability, which may produce dangerous situations. The proposed scheme requires only the measurement of the wheel's angular speed, which can be implemented with low-cost sensors.

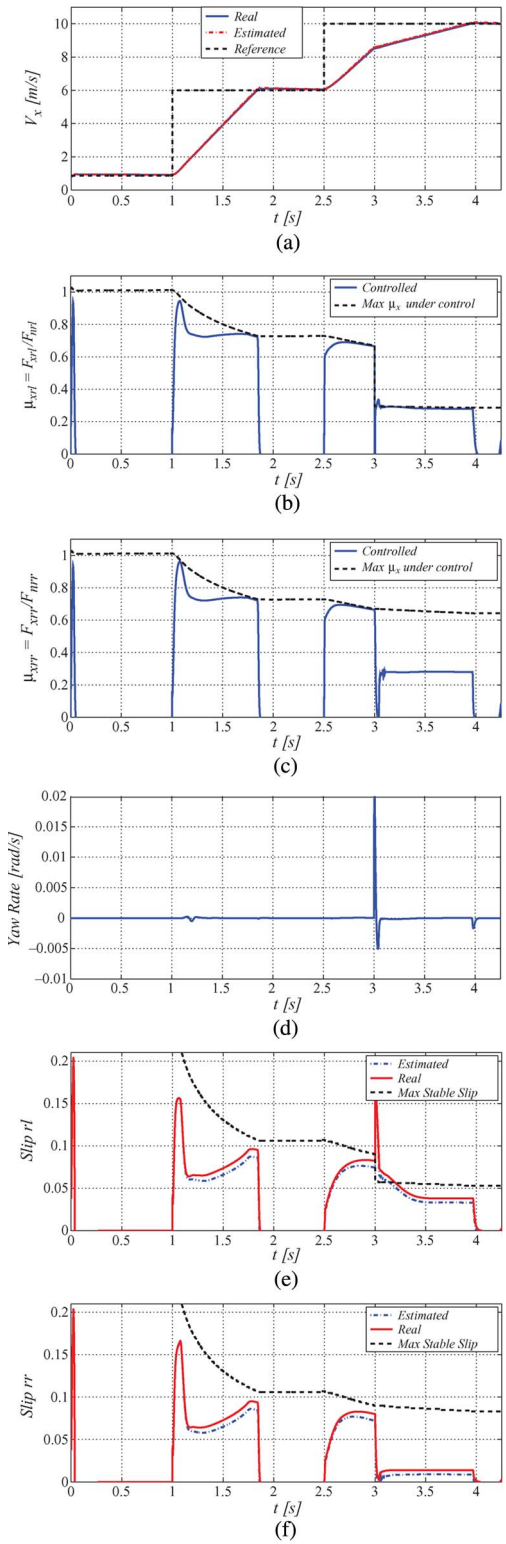


Fig. 14. Experiment C. (a) Linear velocity. (b) Rear-left wheel friction. (c) Rear-right wheel friction. (d) Yaw rate. (e) Slip on the rear-left wheel. (f) Slip on the rear-right wheel.

Simulation results have been presented to demonstrate the feasibility of the proposed control strategy. These results show that the strategy is able to maximize the traction force in each drive wheel during vehicle acceleration, for any road condition, avoiding wheel skidding.

An equal traction force strategy has also been proposed to avoid the production of dangerous yaw rate in situations where the road conditions on each side of the vehicle are different. This proposal allows minimizing the undesired yaw moment when the vehicle travels in a straight line, bringing higher stability at the expense of losing some acceleration capacity but maintaining both drive wheels in the stable adherence zone.

The good performance and the robustness of the proposed observer allows using the estimated variables to implement advanced traction control and vehicle stabilization strategies, without using expensive sensors.

The authors hope this paper can contribute to the development of more advanced strategies for traction and stability control of high-performance EVs.

## REFERENCES

[1] Y. Hori, Y. Toyoda, and Y. Tsuruoka, "Traction control of electric vehicle: Basic experimental results using the test EV 'UOT electric march'," *IEEE Trans. Ind. Appl.*, vol. 34, no. 5, pp. 1131–1138, Sep./Oct. 1998.

[2] H. Sado, S. Sakai, and Y. Hori, "Road condition estimation for traction control in electric vehicle," in *Proc. IEEE ISIE*, 1999, vol. 2, pp. 973–978.

[3] V. Colli, G. Tomassi, and M. Scarano, "Single wheel longitudinal traction control for electric vehicles," *IEEE Trans. Power Electron.*, vol. 21, no. 3, pp. 799–808, May 2006.

[4] D. Yin, S. Oh, and Y. Hori, "A novel traction control for EV based on maximum transmissible torque estimation," *IEEE Trans. Ind. Electron.*, vol. 56, no. 6, pp. 2086–2094, Jun. 2009.

[5] L. Ray, "Nonlinear state and tire force estimation for advanced vehicle control," *IEEE Trans. Control Syst. Technol.*, vol. 3, no. 1, pp. 117–124, Mar. 1995.

[6] L.-Y. Hsu and T.-L. Chen, "Vehicle full-state estimation and prediction system using state observers," *IEEE Trans. Veh. Technol.*, vol. 58, no. 6, pp. 2651–2662, Jul. 2009.

[7] W. Cho, J. Yoon, S. Yim, B. Koo, and K. Yi, "Estimation of tire forces for application to vehicle stability control," *IEEE Trans. Veh. Technol.*, vol. 59, no. 2, pp. 638–649, Feb. 2010.

[8] C. Canudas-de Wit, M. Petersen, and A. Shiriaev, "A new nonlinear observer for tire/road distributed contact friction," in *Proc. 42nd IEEE Conf. Decision Control*, Dec. 2003, vol. 3, pp. 2246–2251.

[9] W.-Y. Wang, I.-H. Li, M.-C. Chen, S.-F. Su, and S.-B. Hsu, "Dynamic slip ratio estimation and control of antilock braking systems using an observer based direct adaptive fuzzy neural controller," *IEEE Trans. Ind. Electron.*, vol. 56, no. 5, pp. 1746–1756, May 2009.

[10] C. Canudas-de Wit, P. Tsiotras, E. Velenis, M. Basset, and G. Gissinger, "Dynamic friction models for road/tire longitudinal interaction," *Veh. Syst. Dyn.*, vol. 39, no. 3, pp. 189–226, Mar. 2003.

[11] N. Patel, C. Edwards, and S. Spurgeon, "A sliding mode observer for tyre friction estimation during braking," in *Proc. Amer. Control Conf.*, Jun. 2006, pp. 5867–5872.

[12] A. Rabhi, N. M'Sirdi, and A. Elhajjaji, "Estimation of contact forces and tire road friction," in *Proc. Mediterranean Conf. Control Autom.*, Jun. 2007, pp. 1–6.

[13] H. Shraim, B. Ananou, L. Fridman, H. Noura, and M. Ouladsine, "Sliding mode observers for the estimation of vehicle parameters, forces and states of the center of gravity," in *Proc. 45th IEEE Conf. Decision Control*, Dec. 2006, pp. 1635–1640.

[14] G. A. Magallán, C. H. De Angelo, and G. O. García, "A neighborhood electric vehicle development with individual traction on rear wheels," *Int. J. Elect. Hybrid Veh.*, vol. 2, no. 2, pp. 115–136, Oct. 2009.

[15] H. Pacejka and R. S. Sharp, "Shear force development by pneumatic tyres in steady state conditions: A review of modelling aspects," *Veh. Syst. Dyn.*, vol. 20, no. 3/4, pp. 121–176, 1991.

[16] C. Canudas de Wit, H. Olsson, K. Astrom, and P. Lischinsky, "A new model for control of systems with friction," *IEEE Trans. Autom. Control*, vol. 40, no. 3, pp. 419–425, Mar. 1995.

[17] S. Hui and S. H. Zack, "Observer design for systems with unknown inputs," *Int. J. Math. Comput. Sci.*, vol. 15, no. 4, pp. 431–436, 2005.

[18] C. Edwards and S. K. Spurgeon, "On the development of discontinuous observers," *Int. J. Control*, vol. 59, no. 5, pp. 1211–1229, May 1994.

[19] J. Xiang, H. Su, and J. Chu, "On the design of Walcott-Zak sliding mode observer," in *Proc. Amer. Control Conf.*, Jun. 2005, vol. 4, pp. 2451–2456.
[20] T. Floquet, C. Edwards, and S. K. Spurgeon, "On sliding mode observers for systems with unknown inputs," *Int. J. Adapt. Control Signal Process.*, vol. 21, no. 8/9, pp. 638–656, Oct./Nov. 2007.
[21] M. Dempsey, "Dymola for multi-engineering modelling and simulation," in *Proc. IEEE VPPC*, Sep. 2006, pp. 1–6.
[22] L. Silva, G. Magallán, C. De Angelo, and G. Garcia, "Vehicle dynamics using multi-bond graphs: Four wheel electric vehicle modeling," in *Proc. 34th IEEE IECON*, Nov. 2008, pp. 2846–2851.

**Guillermo A. Magallan** (S'08) received the Electronic Engineer degree from the Universidad Tecnológica Nacional, Paraná, Argentina, in 2002 and the Dr.Eng. degree from the Universidad Nacional de Río Cuarto, Río Cuarto, Argentina, in 2010.

In 2005, he joined the Grupo de Electrónica Aplicada, Universidad Nacional de Río Cuarto. He is currently with AMETEK Programmable Power, Inc., San Diego CA. His research interests include traction control of electric vehicles, electric motor control, digital-signal-processor-based implementation, and power electronics.

**Cristian H. De Angelo** (S'96–M'05–SM'10) received the Electrical Engineer degree from the Universidad Nacional de Río Cuarto, Río Cuarto, Argentina, in 1999 and the Dr.Eng. degree from the Universidad Nacional de La Plata, La Plata, Argentina, in 2004.

In 1994, he joined the Grupo de Electrónica Aplicada, Universidad Nacional de Río Cuarto. He is also with the Consejo Nacional de Investigaciones Científicas y Técnicas, Buenos Aires, Argentina. His research interests are fault diagnosis of electric machines, sensorless motor control, electric vehicles, and renewable-energy generation.

**Guillermo O. García** (M'86–S'90–M'95–SM'01) received the Electrical and Electronics Engineering degree from the Universidad Nacional de Córdoba, Córdoba, Argentina, in 1981 and the M.Sc. and Dr. degrees in electrical engineering from Universidade Federal do Rio de Janeiro, Rio de Janeiro, Brazil, in 1990 and 1994, respectively.

Since 1994, he has been with the Universidad Nacional de Río Cuarto, Río Cuarto, Argentina, where he is currently the Director of the Grupo de Electrónica Aplicada. He is also with the Consejo Nacional de Investigaciones Científicas y Técnicas, Buenos Aires, Argentina. His research interests include power electronics, electric vehicles, and renewable-energy conversion.